

Dynamic T2 mapping by multi-spin-echo spatiotemporal encoding

Document Version:

Accepted author manuscript (peer-reviewed)

Citation for published version:

Bao, Q, Ma, L, Liberman, G, Solomon, E, Martinho, RP & Frydman, L 2020, 'Dynamic T2 mapping by multi-spin-echo spatiotemporal encoding', *Magnetic Resonance in Medicine*, vol. 84, no. 2, pp. 895-907.
<https://doi.org/10.1002/mrm.28158>

Total number of authors:

6

Digital Object Identifier (DOI):

[10.1002/mrm.28158](https://doi.org/10.1002/mrm.28158)

Published In:

Magnetic Resonance in Medicine

License:

Other

General rights

@ 2020 This manuscript version is made available under the above license via The Weizmann Institute of Science Open Access Collection is retained by the author(s) and / or other copyright owners and it is a condition of accessing these publications that users recognize and abide by the legal requirements associated with these rights.

How does open access to this work benefit you?

Let us know @ library@weizmann.ac.il

Take down policy

The Weizmann Institute of Science has made every reasonable effort to ensure that Weizmann Institute of Science content complies with copyright restrictions. If you believe that the public display of this file breaches copyright please contact library@weizmann.ac.il providing details, and we will remove access to the work immediately and investigate your claim.

Dynamic T₂ mapping by multi-spin-echo spatiotemporal encoding

Qingjia Bao, Lingceng Ma,[#] Gilad Liberman, Eddy Solomon, Ricardo P. Martinho and Lucio Frydman*

Department of Chemical and Biological Physics, Weizmann Institute, Rehovot 76100, Israel

Keywords: quantitative T2 mapping, abdominal imaging, breast MRI, multi-spin-echo sequences, spatiotemporal encoding

Abbreviations: DCE, dynamic contrast enhanced; EPI, Echo Planar Imaging; MSE, multi-spin-echo; SE, spin echo; SPEN, spatiotemporal encoding; SS, single-shot

Running Title: *Quantitative 2D single-shot T2 mapping*

Word count: 3,302

Figures: 10 in the main text; 2 in the Supporting Information

Tables: 1 in the Supporting Information

Equations: 4

References: 51

[#]On leave from: Department of Electronic Science, Fujian Provincial Key Laboratory of Plasma and Magnetic Resonance, Xiamen University, Xiamen 361005, China

*Prof. Lucio Frydman; +972-8-9344903; lucio.frydman@weizmann.ac.il

Abstract

Purpose: To develop a pulse sequence for acquiring robust, quantitative T_2 relaxation maps in real time.

Methods: The pulse scheme relies on fully-refocused spatiotemporally encoded multi-spin-echo trains, which provide images that are significantly less distorted than spin-echo EPI-based counterparts. This enables single-shot T_2 mapping in inhomogeneity-prone regions. Another advantage of these schemes stems from their ability to interleave multiple scans in a reference-free fashion, providing an option to increase sensitivity and spatial resolution with minimal motional artifacts.

Results: The method was implemented in preclinical and clinical scanners, where single-shot acquisitions delivered reliable T_2 maps in ≤ 200 ms with $\approx 250\mu\text{m}$ and ≈ 3 mm resolutions, respectively. Ca. 4 times higher spatial resolutions were achieved for the motion-compensated interleaved versions of these acquisitions, delivering T_2 maps in ca. 10 seconds per slice. These maps were nearly indistinguishable from multi-scan relaxometric maps requiring orders-of-magnitude longer acquisitions; this was confirmed by mice head and real-time mice abdomen 7T scans performed following contrast-agent injections, as well as by 3T human brain and breast scans.

Conclusion: This study introduced and demonstrated a new approach for acquiring rapid and quantitative T_2 data, which is particularly reliable when operating at high fields and/or targeting heterogeneous organs or regions.

Introduction

Although MRI is widely appreciated thanks to its delivery of fine anatomical details, even further information can become available if its signal intensities are modulated by contrast mechanisms conveying information about chemistry and/or microstructure (1–7). Quantitative relaxometry measurements that isolate the contributions of NMR contrast mechanisms such as T_1 or T_2 can, with or without the use of exogenous contrast agents, enhance these maps, and reveal biophysical and physiological properties going beyond those of a density-based image (8). In particular, quantitative T_2 relaxation evaluations have become increasingly important in a variety of research and clinical applications, including studies of iron overload (9,10), of stroke (11,12), to analyze cartilage diseases (13,14), and in multiple sclerosis (15). In general, traditional T_2 relaxometry involves the acquisition of several echoed images at various spin-echo times TE; this results in relatively long scan times, as well as on an increased susceptibility to subject motion. This in turn leaves important potential research and diagnosis areas benefiting from the real-time mapping of relaxation parameters, including both physiological and functional applications, in need for faster mapping tools (16,17). Various acquisition and processing methods have been proposed to overcome this problem. These include reducing the number of encodings without image sacrifices based on sparse sampling (18) and on parallel imaging (19) –including undersampled spin-echoes (20) and compressed sensing (21). Additional constraints used to shorten these acquisitions include considering the sparsity of the T_2 -weighted images (22,23), the low-rank properties of the image series (24), as well as model-based reconstructions (25). Even with such optimizations these approaches require multiple shots, leading to overall acquisitions that are several seconds-to-minutes long, thus rendering real-time T_2 mapping difficult. On the other hand, single shot experiments based on EPI can deliver *in vivo* images in 100s of milliseconds; when endowed with the possibility of detecting multiple echoes, EPI- and gradient- and spin-echo (GRASE) approaches have been used to collect T_2 maps in one or two scans (26–28). A limitation of these recently developed single-shot (SS) T_2 mapping protocols is that their acquired data are usually distorted, as a result of relying on sequences that, like EPI, are sensitive to the presence of B_0 field heterogeneities (29).

This study explores an alternative approach to SS T_2 mapping, based on the acquisition of spatiotemporally encoded (30–32), multi-spin-echo (MSE, 33) trains. Thanks to its reliance on a direct spatial acquisition that overcomes traditional Nyquist criteria, SPEN enables the use of

strong gradients along the low-bandwidth dimension; freedom from Nyquist constraints can also assist in improving an image resolution by relying on restricted Field-of-Views (FOVs) free from aliasing artifacts (30,34). Further resilience to image distortions arising from B_0 or shift heterogeneities arises from the possibility of collecting SPEN in so-called “fully refocused” acquisitions, whereby sequential points along the reconstructed image are largely freed from T_2^* effects (35,36). A further advantage of this space-based image acquisition mode stems from its ability to interleave multiple scans in a reference-free fashion, giving the option of increasing sensitivity and resolution with minimal motional complications (32,37). The consequences of combining all these features with multiple echoes into an experiment to map T_2 s is here explored – first in phantoms, where it is used to corroborate its reliability under ideal acquisition conditions. Tests in rodent brains showed multi-spin-echo SPEN’s (MSE-SPEN) superiority over EPI-based counterparts, particularly when dealing with inhomogeneity-challenged regions; in fact upon data interleaving, SPEN’s T_2 maps were nearly indistinguishable from multi-scan relaxometric maps requiring order-of-magnitude longer acquisitions. Real-time T_2 maps could also be collected on the abdomen of mice subject to contrast-agent injections, under conditions for which no meaningful EPI data resulted. The sequences were also translated into clinical scanners, where they were found to deliver equally faithful data for human brain scans. The potential of this new method and the possibility to incorporate into it more advanced extensions, are briefly discussed.

Methods

Sequence Design Considerations. The single shot T_2 -mapping pulse sequence here developed is shown in Figure 1a. This is based on the so-called hybrid SPEN acquisition mode, whereby the swept chirped pulse is used to image the low bandwidth dimension usually associated with EPI’s phase-encoding for overcoming the latter’s inhomogeneity, while the orthogonal read-out direction is acquired in the usual k-space fashion. Additional robustness is achieved by executing the acquisition under fully refocused conditions, where contributions to the final images are devoid from major T_2^* effects (35). The effects of T_2 throughout the course of this acquisition will still be present, yet they will not affect all elements in the image equally. To visualize this we consider for concreteness that the chirped pulse generating the SPEN encoding, involves an inversion pulse sweeping a bandwidth BW during a time T_e while in the presence of a y -axis G_e gradient. This will impart an encoding phase

$$\varphi_e(y) = -\frac{(\gamma G_e)^2}{R} \left(\frac{FOV_y}{2} + y \right)^2 \quad (1)$$

where $R = BW / T_e = \gamma G_e FOV_y / T_e$ is a sweep rate defined by the targeted field-of-view FOV_y , and $-FOV_y / 2$ is an initial position defined by both the encoding pulse and the action of a pre-acquisition gradient of area $k_{pre} = \gamma G_e T_e$. During the acquisition, the signal is monitored as a function of an acquisition time t while under the action of an acquisition gradient G_{acq} that for simplicity we consider constant, leading to a total phase

$$\Phi(y, t) = \varphi_e(y) + \gamma G_{acq} t y = -\frac{(\gamma G_e)^2}{R} \left(\frac{FOV_y}{2} + y \right)^2 + \gamma G_{acq} t y \quad (2)$$

As spins near the stationary-phase point $\frac{\partial[\varphi_e(y) + \gamma G_{acq} t y]}{\partial y} = 0$ dominate the resulting signals,

the sample's density is probed in a point-wise manner as different positions y_{SP} fulfill the stationary-phase condition $y_{SP}(t) = -\frac{FOV_y}{2} + FOV_y \left(\frac{t}{T_a} \right)$. The images are thus obtained by a non-

Fourier analysis of the signal's magnitude (38), whose sampling progresses from $-\frac{FOV_y}{2}$ at time $t=0$

to $+\frac{FOV_y}{2}$ when $t=T_a$. While setting $G_{acq}=G_e$ and $T_a=2T_e$ ensures that T_2^* effects for all $y_{SP}(t)$

positions will be null, it also follows that this progression will lead to minimal T_2 weightings for the $-\frac{FOV_y}{2}$ end of the image, to a maximal T_2 decay for its $+\frac{FOV_y}{2}$ counterpart. As the actual T_2

values cannot be computed from such single weighted-image measurement, the sequence in Figure 1a incorporates a spin-echo train whereby multiple SPEN images are collected as a function of different transverse evolution times. These spin-echoes are assumed as arising from a series of short, broad-banded 180° refocusing pulses; as a result of these, the positions of minimal and maximal T_2 decays will switch in space between consecutive data sets. To visualize the origin of this alternation consider the phase $\Phi(y, t=T_a)$ at the conclusion of the first image acquisition:

$$\Phi(y, t=T_a) = -\frac{(\gamma G_e)^2}{R} \left(\frac{FOV_y}{2} + y \right)^2 + \gamma G_{acq} T_a y \quad (3)$$

Assuming that the effects of the hard echoing pulse equals to a change of sign in the spin evolution phase, and keeping in mind that the last term in Eq. (3) also equals $2\gamma G_e T_e y$, the phase arising over the course of the second SPEN image acquisition can be written as

$$\Phi_{2nd}(y) = \frac{(\gamma G_e)^2}{R} \left(\frac{FOV_y}{2} - y \right)^2 + \gamma G_{acq} T_a y \quad (4)$$

The position of y_{SP} for this second acquisition can be calculated as above, leading to a rasterization of positions given by $y_{SP}(t) = \frac{FOV_y}{2} - FOV_y \left(\frac{t}{T_a} \right)$ as a function of the second acquisition time $0 \leq t \leq T_a$. Similarly, if another hard 180° pulse is applied and a third SPEN image is acquired, another reversal will follow and the situation will revert back to the first-image acquisition (Figs. 1a, 1b). This alternating reading out of the y-axis yields a T_2 weighting that is not as in conventional MSE sequences, and will lead to uneven TE samplings unless located in the $y=0$ center of the image. Yet these timing variations can be accounted for, leading to accurate T_2 maps if suitably considered.

Image Processing Considerations. Figures 2 and 3 show the full pulse sequence and data processing flow chart used in this study. The sequence involved up to four concentric loops (Fig. 2); from inner- to outer-most these include an oscillating readout acquisition delivering the 2D SPEN image, an MSE loop encoding the T_2 information, a multi-slice loop extending this information into a third dimension, and an optional multi-shot loop used for eventual interleaving and thereby resolution improvement along the SPEN dimension (37,39-41). The corresponding data processing flow chart (Fig. 3) started with a Fourier Transform (FT) along the readout dimension. Then, even/odd echo train data sets were separated and processed independently via a super-resolution transformation (42,43), accounting for the blurring incurred by the parabolic phases and including a self-referenced correction to overcome imperfections of the gradient system or motion-related issues (32,40). As the direction along which space is rasterized is different for even and odd echo sets along the SPEN dimension, images of the even echoes were flipped to achieve a consistent image orientation. Finally, the echo times for different positions along the SPEN direction were suitably computed as per the arguments in the preceding paragraph, and mono-exponential fittings of the resulting images were used to calculate the T_2 value on a per-voxel basis.

Animal and Human Scanning. Phantom and animal-based acquisitions were carried out on a 7T/120mm horizontal magnet MRI using a quadrature 40mm Millipede[®] volume coil (Agilent Technologies, Santa Clara, CA). Animal protocols and maintenance were done in accordance with guidelines of the Institutional Committee on Animals of the Weizmann Institute of Science (IACUC protocol 10790514), which is fully accredited by the AAALAC, the US NIH Office of Laboratory Animal Welfare, and the Israel Ministry of Health. Mice were anesthetized with isoflurane (1-2%) via a vaporizer, and the animals' body temperatures were maintained constant

by using a water-based heating system. Respiration was monitored via a pressure sensor (SA-II, Stony Brook, NY) and maintained at 30–50 breaths per minute; animals were not mechanically fixed in any of the experiments. Fast spin echo, SE-EPI and gradient echo experiments were carried out using sequences from the scanner’s library; all EPI acquisitions required additional reference scans to correct for even/odd imperfections. The MSE-SPEN sequence in Figure 2 was written in the Varian’s VNMRJ 3.2 imaging environment, as well as in Siemens’ VE11C programming environment. The latter was used to scan human volunteers on a 3T Prisma Siemens MRI (Erlangen, Germany), using either a 20-channel head or a 12-channel breast coil. These human experiments were approved by the Internal Review Boards of Wolfson Medical Center (WOMC-0091-11, Holon, Israel) and of the Weizmann Institute, and were collected after obtaining suitable informed consents. Table S1 in the Supporting Information gives an overall summary of the experiments carried out for this study; the exact parameters used for setting up the various experiments are detailed in the corresponding figure’s captions. Image reconstructions and T_2 maps were done for all acquisition schemes using custom-written Matlab® packages; all these sequences and macros are available upon request from https://www.weizmann.ac.il/chemphys/Frydman_group/software.

Results

Figure 4 shows a series of experimental results obtained for an aqueous phantom containing tubes with different Gd-DTPA concentrations, inserted inside a larger containing tube. Shown are the first-echo images (top) and the T_2 maps (bottom) arising from a variety of pulse sequences, including SS-MSE-EPI and SS-MSE-SPEN, interleaved MSE-EPI, interleaved MSE-SPEN, conventional single-spin-echo (SE) MRI data collected as a function of different echo times, and multi-spin-echo (MSE) conventional MRI. These comparisons show that all sequences can provide reasonable T_2 maps for the various solutions despite differing by several orders of magnitude in their overall data acquisition times. An improvement in sensitivity with the number of scans is also evident in the interleaved acquisitions; worth remarking as well is the remarkably higher immunity to B_0 inhomogeneities –mostly due to the interface between the different tubes making up the phantom– displayed by the SPEN images over their EPI counterparts. Likewise, the T_2 values obtained with both SS- and interleaved SPEN are in considerably better agreement with

those afforded by the SE MRI data, than what can be achieved from the lower quality EPI-derived images. Moreover, SPEN's multi-shot scheme provides high-resolution T_2 maps in around 10 seconds, nearly indistinguishable from those arising from much longer SE or MSE acquisitions.

Figure 5 extends these phantom comparisons to an *in vivo* setting, exploring the behavior of the different T_2 mapping experiments on a mouse brain. The number of echoes in these experiments is smaller than in the phantom cases owing to the shorter overall T_2 s; yet again, in comparison to the EPI data, the SPEN images have higher quality and make it possible to achieve T_2 maps with more accurate anatomical features. Notice in particular the distorted regions highlighted by arrows in the EPI images, appearing distortion-free in the SPEN counterparts. Furthermore, the SPEN-derived images and maps display clear similarities to those arising from lengthy MSE acquisitions, yet provide these high resolution maps in under a minute and thereby in timescales compatible with dynamic studies.

Figure 6 presents another set of *in vivo* brain scans, this time arising from a human volunteer. Unlike the previous examples this scan involved a multi-slice acquisition, facilitated in the SPEN cases by the even number of 180° inversion pulses involved in the MSE trains. Once again, there is good correspondence between the SPEN-based acquisition and the longer multi-scan ones. In such instances, however, the larger volumes involved and the high optimization of the human scanner towards brain acquisitions, makes the differences between EPI- and SPEN-based acquisitions less remarkable than for the preclinical counterpart.

Homogeneity within the brain is relatively high, and so differences between SPEN and EPI data are relatively minor; mostly these are restricted to attenuations in distortions and pile-ups affecting the EPI images –particularly the single-shot ones– in the frontal area. A more serious challenge is posed by the exams introduced in Figure 7, focusing on human scans on single breasts. Here the intimate mixing of fat and water, plus the presence of sizable, unavoidable respiratory and cardiac motions, complicate the acquisition of EPI-based data. By contrast, better overall T_2 -weighted images and T_2 maps that more closely correlate with the results arising from multi-scan, multi-echo acquisitions, arise upon utilizing SPEN. Notice that the latter measurements also exploited SPEN's ability to zoom into a region of interest (in the present case a single breast) without folding complications.

Besides dealing well with field inhomogeneities, one of the potential advantages of the MSE-SPEN experiment rests in its ability to overcome motion artifacts: the ca. 100-200 ms

involved by the T_2 mapping of the SS-MSE-SPEN experiments (with the actual duration depending on the number of echoes in the train), allow one to disregard motions altogether. For the interleaved variants, motion-derived instabilities can arise, but these can be partially compensated thanks to the fact that each shot in interleaved SPEN provides a low-resolution but fully unfolded image. By correcting scan-to-scan phase instabilities arising from motion, high-resolution and largely motion-artifact-free T_2 -weighted maps can become available. This is exemplified in Figure 8 which focuses on *in vivo* T_2 mapping of a mouse's kidney—a kind of scan which can be notoriously challenging in delivering faithful data because of motion issues. Figure 8a compares T_2 -weighted images arising from interleaved EPI and SPEN acquisitions, against a regular multi-scan alternative. All images reveal various main parts of the kidney; it also appears that out of all the acquisitions alternatives interleaved SPEN provides the crispiest images, a consequence of combining robustness against field inhomogeneities with short acquisition times that provide better immunity against abdominal motions. Figure 8b shows multi-slice T_2 images and maps arising from MSE-SPEN acquisitions collected in around 10 seconds each. These clearly reveal the different relaxivities of various components including external and internal cortex layers, the medulla region and the collecting ducts.

The faithfulness of these images and the rapid nature of the T_2 mapping procedures also allows one to follow the changes in kidney relaxivity in near-real-time—something that can be useful for elucidating functional or perfusion characteristics. This is further illustrated in Figure 9, where the latter scenario was investigated by administering a contrast agent to a live anesthetized mouse, and interleaved MSE-SPEN was used to generate high resolution 2D maps of the animal's T_2 changes (Fig. 9a-d), with a time resolution of 2 seconds. The various panels in this figure show results observed before and after the injection of a Gd-DTPA bolus. The animal's kidneys evidence a clearly visible, generic T_2 shortening during the wash-in of the contrast bolus, and a subsequent T_2 lengthening with its washout (Fig. 9c). These dynamics were different for different regions, with the kidney's cortex exhibiting lower basal end-levels than the medulla. The behavior attained by the MSE-SPEN method-based dynamic T_2 mapping are in good agreement with those of standard T1w DCE measurements (Figs. 9d, 9e).

Discussion and Conclusions

This study examined a spatiotemporally encoded approach for acquiring rapid, quantitative T_2 maps, involving single- and multi-shot scans. From a point of view of reliability, it was found that hybrid SPEN-based sequences could yield better results than EPI counterparts –particularly when operating at higher fields and heterogeneous regions outside the human brain. By incorporating simple, referenceless interleaving procedures, these maps could be collected in just a few seconds with $\approx 1\text{mm}$ in-plane resolution on humans and $\approx 0.12\text{mm}$ resolutions on animals. The results delivered were quantitatively comparable with much longer multi-scan acquisitions, further attesting their reliability. This can be appreciated from the data presented in Figure 10, summarizing the T_2 analyses arising from the various *in vivo* experiments presented in this work. As can be appreciated, good agreement is here evidenced between the values arising from the various SPEN experiments, and the lengthier multi-scan MSE determinations serving as “gold standard” for these T_2 measurements. Additional details about these *in vivo* comparisons are summarized in Figures S1 and S2 of the Supporting Information.

The dependability of these T_2 maps, however, may be impaired if, by contrast to what happens in the preclinical and human studies performed here, B_1^+ homogeneity is deficient; in such cases, MSE trains may be spatially biased by imperfections in the repeated pulses. Such imperfections might be taken into account *a priori* from B_1 field maps arising from the RF coil, or by use of better compensated refocusing strategies –for instance adiabatic inversions, super-cycling or composite pulses (44,45). Another complicating factor may arise upon porting these MSE experiments to higher fields, characterized by shorter T_2 s and therefore with a more limited capacity to accommodate multiple echoes; given SPEN’s reliance on frequency-swept pulses and on a progressive image acquisition, this will place a lower bound limit on the kind of T_2 s that the methods discussed in this study can tackle. Still, data interleaving procedures of the kind used in this work, leading to a shortening of the effective acquisition times per scan, may alleviate this. Also associated with a porting of the experiments to higher fields is the deposition of higher RF powers (SAR), a problem which affects SPEN more severely than EPI counterparts(29,46–48). SPEN’s SAR load, however, derives mostly from the initial frequency swept encoding pulse, which is only used once in either the conventional or in the MSE versions here introduced for T_2 mapping.

To evaluate the potential of the new approach, both phantom as well as *in vivo* T_2 maps were collected on animals and humans. The phantom experiments evidenced the good quantitative

reliability of the MSE-SPEN approach, while the *in vivo* ones explored some of its applications. Most interesting among these was the mapping of abdominal organs in mice; once extended to humans, we trust that this approach will also serve useful clinical aims in examining challenging organs such as prostate. Additional interesting extensions of these fast methods involves their melding with other potential sources of contrast –particularly with T_1 and with diffusivity information. Such sources of complementary information would normally require nested multidimensional encodings for establishing correlations among them (49–51); this of course would be greatly facilitated under realistic *in vivo* conditions, if the encoding of the imaging and the T_2 information would arise in a fast, sub-minute timescale. Further compressions could result if the effects of the multi-echoing being used for the T_2 mapping, is factored into the T_1 -weighting that's imparted in SPEN's multi-slicing procedure: a compressed sensing approach could then be used to simultaneously extract T_1 and T_2 maps from the ensuing data. These additional applications and developments are currently under study.

Acknowledgments. We are grateful to Mr. Koby Zibzener (Weizmann Institute) for technical assistance, to Dr. Zhiyong Zhang for valuable discussions, and to Dr. Sagit Shushan (Wolfson Medical Center), Dr. Edna Haran, Mr. Martins Otikovs and the Weizmann MRI technician team, for assistance in the human imaging scans. Financial support from the Israel Science Foundation through grants ISF 965/18 and ISF/NSFC grant 2508/17, the EU Horizon 2020 program (Marie Skłodowska-Curie Grant 642773), the Kimmel Institute for Magnetic Resonance and the generosity of the Perlman Family Foundation, are also acknowledged. LM thanks the Chinese Science Council (grant 201806310085) and the Israeli Planning and Budget Committee for graduate fellowships.

References:

1. Ma D, Gulani V, Seiberlich N, Liu K, Sunshine JL, Duerk JL, Griswold MA. Magnetic resonance fingerprinting. *Nature* 2013;495:187–192. doi: 10.1038/nature11971.
2. Cercignani M, Bouyagoub S. Brain microstructure by multi-modal MRI: Is the whole greater than the sum of its parts? *Neuroimage* 2017;1–11. doi: 10.1016/j.neuroimage.2017.10.052.
3. Tofts P. *Quantitative MRI of the Brain*. Chichester: Wiley; 2018. doi: 10.1201/b21837.
4. Ciccarelli O, Toosy AT, De Stefano N, Wheeler-Kingshott CAM, Miller DH, Thompson AJ. Assessing Neuronal Metabolism In Vivo by Modeling Imaging Measures. *J. Neurosci.* 2010;30:15030–15033. doi: 10.1523/JNEUROSCI.3330-10.2010.
5. Edwards LJ, Kirilina E, Mohammadi S, Weiskopf N. Microstructural imaging of human neocortex in vivo. *Neuroimage* 2018;182:184–206. doi: 10.1016/j.neuroimage.2018.02.055.
6. Langkammer C, Bredies K, Poser BA, Barth M, Reishofer G, Fan AP, Bilgic B, Fazekas F, Mainero C, Ropele S. Fast quantitative susceptibility mapping using 3D EPI and total generalized variation. *Neuroimage* 2015;111:622–630. doi: 10.1016/j.neuroimage.2015.02.041.
7. Möller HE, Bossoni L, Connor JR, Crichton RR, Does MD, Ward RJ, Zecca L, Zucca FA, Ronen I. Iron, Myelin, and the Brain: Neuroimaging Meets Neurobiology. *Trends Neurosci.* 2019:1–18. doi: 10.1016/j.tins.2019.03.009.
8. Margaret Cheng HL, Stikov N, Ghugre NR, Wright GA. Practical medical applications of quantitative MR relaxometry. *J. Magn. Reson. Imaging* 2012;36:805–824. doi: 10.1002/jmri.23718.
9. Langkammer C, Krebs N, Goessler W, Scheurer E, Ebner F, Yen K, Fazekas F, Ropele S. Quantitative MR Imaging of Brain Iron: A Postmortem Validation Study. *Radiology* 2010;257:455–462. doi: 10.1148/radiol.10100495.
10. Pierre TGS, Clark PR, Chua-anusorn W, Fleming AJ, Jeffrey GP, Olynyk JK, Pootrakul P, Robins E, Lindeman R. Noninvasive measurement and imaging of liver iron concentrations using proton magnetic resonance. 2005;105:855–861. doi: 10.1182/blood-2004-01-0177.
11. Bernarding J, Braun J, Hohmann J, Mansmann U, Hoehn-Berlage M, Stapf C, Wolf KJ, Tolxdorff T. Histogram-based characterization of healthy and ischemic brain tissues using multiparametric MR imaging including apparent diffusion coefficient maps and relaxometry. *Magn. Reson. Med.* 2000;43:52–61. doi: 10.1002.
12. Siemonsen S, Mouridsen K, Holst B, Ries T, Finsterbusch J, Thomalla G, Ostergaard L, Fiehler J. Quantitative T2 values predict time from symptom onset in acute stroke patients. *Stroke* 2009;40:1612–1616. doi: 10.1161/STROKEAHA.108.542548.
13. Welsch GH, Hennig FF, Krinner S, Trattng S. T2 and T2* Mapping. *Curr. Radiol. Rep.* 2014;2:60. doi: 10.1007/s40134-014-0060-1.
14. Mamisch TC, Trattng S, Quirbach S, Marlovits S, White LM, Welsch GH. Quantitative T2 Mapping of Knee Cartilage: Differentiation of Healthy Control Cartilage and Cartilage Repair Tissue in the Knee with Unloading—Initial Results. *Radiology* 2010;254:818–826. doi: 10.1148/radiol.09090335.
15. MacKay AL, Vavasour IM, Rauscher A, Kolind SH, Mädler B, Moore GRW, Traboulsee AL, Li DKB, Laule C. MR Relaxation in Multiple Sclerosis. *Neuroimaging Clin. N. Am.* 2009;19:1–26. doi: 10.1016/j.nic.2008.09.007.
16. Lawrence SJD, Formisano E, Muckli L, de Lange FP. Laminar fMRI: Applications for cognitive neuroscience. *Neuroimage* 2019;197:785–791. doi: 10.1016/j.neuroimage.2017.07.004.
17. Niendorf T, Frydman L, Neeman M, Seeliger E. Google maps for tissues: Multiscale imaging of biological systems and disease. *Acta Physiol.* 2019:1–5. doi: 10.1111/apha.13392.
18. Lustig M, Donoho D, Pauly JM. Sparse MRI: The application of compressed sensing for rapid MR

- imaging. *Magn. Reson. Med.* 2007;58:1182–1195. doi: 10.1002/mrm.21391.
19. Deshmane A, Gulani V, Griswold MA, Seiberlich N. Parallel MR imaging. *J. Magn. Reson. Imaging* 2012;36:55–72. doi: 10.1002/jmri.23639.
 20. Ben-Eliezer N, Sodickson DK, Shepherd T, Wiggins GC, Block KT. Accelerated and motion-robust in vivo T2 mapping from radially undersampled data using bloch-simulation-based iterative reconstruction. *Magn. Reson. Med.* 2016;75:1346–1354. doi: 10.1002/mrm.25558.
 21. Velikina J V., Alexander AL, Samsonov A. Accelerating MR parameter mapping using sparsity-promoting regularization in parametric dimension. *Magn. Reson. Med.* 2013;70:1263–1273. doi: 10.1002/mrm.24577.
 22. Jensen JH, Ye JC, Sodickson DK, Feng L, Otazo R, Jung H, Kim D. Accelerated cardiac T2 mapping using breath-hold multiecho fast spin-echo pulse sequence with k-t FOCUSS. *Magn. Reson. Med.* 2011;65:1661–1669. doi: 10.1002/mrm.22756.
 23. Majumdar A, Ward RK. Accelerating multi-echo T2 weighted MR imaging: Analysis prior group-sparse optimization. *J. Magn. Reson.* 2011;210:90–97. doi: 10.1016/j.jmr.2011.02.015.
 24. Peng X, Ying L, Liu Y, Yuan J, Liu X, Liang D. Accelerated exponential parameterization of T2 relaxation with model-driven low rank and sparsity priors (MORASA). *Magn. Reson. Med.* 2016;76:1865–1878. doi: 10.1002/mrm.26083.
 25. Zhao B, Lam F, Liang ZP. Model-based MR parameter mapping with sparsity constraints: Parameter estimation and performance bounds. *IEEE Trans. Med. Imaging* 2014;33:1832–1844. doi: 10.1109/TMI.2014.2322815.
 26. Cai C, Zeng Y, Zhuang Y, et al. Single-Shot T2 Mapping Through Overlapping-Echo Detachment (OLED) Planar Imaging. *IEEE Trans. Biomed. Eng.* 2017;64:2450–2461 doi: 10.1109/TBME.2017.2661840
 27. Cai C, Wang C, Zeng Y, Cai S, Liang D, Wu Y, Chen Z, Ding X, Zhong J. Single-shot T2 mapping using overlapping-echo detachment planar imaging and a deep convolutional neural network. *Magn. Reson. Med.* 2018;1–13. doi: 10.1002/mrm.27205.
 28. Chu ML, Chang HC, Oshio K, Chen NK. A single-shot T2 mapping protocol based on echo-split gradient-spin-echo acquisition and parametric multiplexed sensitivity encoding based on projection onto convex sets reconstruction. *Magn. Reson. Med.* 2018;79:383–393. doi: 10.1002/mrm.26696.
 29. Schmitt K., Stehling R. & Turner FM. Echo-Planar Imaging: Theory, Technique and Application. Springer V. (Heidelberg, editor.). Heidelberg: Springer Verlag; 1998.
 30. Tal A, Frydman L. Single-scan multidimensional magnetic resonance. *Prog. Nucl. Magn. Reson. Spectrosc.* 2010;57:241–292. doi: 10.1016/j.pnmrs.2010.04.001.
 31. Ben-Eliezer N, Frydman L. Spatiotemporal encoding as a robust basis for fast three-dimensional in vivo MRI. *NMR Biomed.* 2011;24:1191–1201. doi: 10.1002/nbm.1673.
 32. Seginer A, Schmidt R, Leftin A, Solomon E, Frydman L. Referenceless reconstruction of spatiotemporally encoded imaging data: Principles and applications to real-time MRI. *Magn. Reson. Med.* 2014;72:1687–1695. doi: 10.1002/mrm.25084.
 33. Bao Q, Solomon E, Liberman G, Cousin S, Fydman L. Single-scan multi-spin-echo SPEN for dynamic T2 mapping and for 3D T2 weighted anatomical imaging. *Proc. 26th Ann. Meet. ISMRM, Paris, France* 2018:380.
 34. Schmidt R, Frydman L. Alleviating artifacts in 1H MRI thermometry by single scan spatiotemporal encoding. *Magn. Reson. Mater. Physics, Biol. Med.* 2013;26:477–490. doi: 10.1007/s10334-013-0372-9.
 35. Schmidt R, Frydman L. New spatiotemporal approaches for fully refocused, multislice ultrafast 2D MRI. *Magn. Reson. Med.* 2014;71:711–722. doi: 10.1002/mrm.24714.
 36. Ben-Eliezer N, Solomon E, Harel E, Nevo N, Frydman L. Fully refocused multi-shot spatiotemporally

- encoded MRI: Robust imaging in the presence of metallic implants. *Magn. Reson. Mater. Physics, Biol. Med.* 2012;25:433–442. doi: 10.1007/s10334-012-0318-7.
37. Schmidt R, Seginer A, Frydman L. Interleaved multishot imaging by spatiotemporal encoding: A fast, self-referenced method for high-definition diffusion and functional MRI. *Magn. Reson. Med.* 2016;75:1935–1948. doi: 10.1002/mrm.25742.
 38. Ben-Eliezer N, Irani M, Frydman L. Super-resolved spatially encoded single-scan 2D MRI. *Magn. Reson. Med.* 2010;63:1594–1600. doi: 10.1002/mrm.22377.
 39. Cousin SF, Liberman G, Solomon E, Otikovs M, Frydman L. A regularized reconstruction pipeline for high-definition diffusion MRI in challenging regions incorporating a per-shot image correction. *Magn. Reson. Med.* 2019;82:1332–1330 doi: 10.1002/mrm.27802.
 40. Bao Q, Liberman G, Solomon E, Lustig M, Fydman L. Diffusion-weighted in vivo imaging with ≤ 100 μm resolution: Principles and applications to ADC mapping of pregnant mice. *Proc. 26th Annu. Meet. ISMRM, Paris, France* 2018:1021.
 41. Liberman G, Solomon E, Lustig M, Frydman L. Multiple-coil k-space interpolation enhances resolution in single-shot spatiotemporal MRI. *Magn. Reson. Med.* 2018;79:796–805. doi: 10.1002/mrm.26731.
 42. Ben-Eliezer N, Irani M, Frydman L. Super-resolved spatially encoded single-scan 2D MRI. *Magn. Reson. Med.* 2010;63:1594–1600. doi: 10.1002/mrm.22377.
 43. Schmidt R, Baishya B, Ben-Eliezer N, Seginer A, Frydman L. Super-resolved parallel MRI by spatiotemporal encoding. *Magn. Reson. Imaging* 2014;32:60–70. doi: 10.1016/j.mri.2013.07.007.
 44. Jang A, Wu X, Auerbach EJ, Garwood M. Designing 3D selective adiabatic radiofrequency pulses with single and parallel transmission. *Magn. Reson. Med.* 2018;79:701–710. doi: 10.1002/mrm.26720.
 45. Kupče Ě, Freeman R. Adiabatic Pulses for Wideband Inversion and Broadband Decoupling. *J. Magn. Reson. Ser. A* 1995;115:273–276. doi: 10.1006/jmra.1995.1179.
 46. Stehling M, Turner R, Mansfield P. Echo-planar imaging: magnetic resonance imaging in a fraction of a second. *Science*. 1991;254:43–50. doi: 10.1126/science.1925560.
 47. Liua X, Fengb Y, Luc ZR, Morrelld G, Jeong EK. Rapid simultaneous acquisition of T1 and T2 mapping images using multishot double spin-echo EPI and automated variations of TR and TE (ms-DSEPI-T12). *NMR Biomed.* 2010;23:97–104. doi: 10.1002/nbm.1440.
 48. Bao Q, Martinho RP, Frydman L. A Fast Multi-slice T1 mapping method based on SPatiotemporal ENcoding. *Proc. 27th Annu. Meet. ISMRM, Montreal, Canada* 2019:4564.
 49. Andrews DA, Campbell JSW, Leppert IR, Park DJ, Pike GB, Jonathan R, Tardif CL. Efficient whole-brain tract-specific T1 mapping with slice-shuffled inversion-recovery diffusion-weighted imaging at 3T. 2019:3–5. doi: 10.1002/hbm.22099.
 50. Staroswiecki E, Granlund KL, Alley MT, Gold GE, Hargreaves BA. Simultaneous Estimation of T 2 and Apparent Diffusion Coefficient in Human Articular Cartilage In Vivo with a Modified Three-Dimensional Double Echo Steady State (DESS) Sequence at 3 T. 2012;1096:1086–1096. doi: 10.1002/mrm.23090.
 51. Aliotta E, Moulin K, Zhang Z, Ennis DB. Simultaneous measurement of T 2 and apparent diffusion coefficient (T 2 +ADC) in the heart with motion-compensated spin echo diffusion-weighted imaging. *Magn. Reson. Med.* 2018; 79:654–662. doi: 10.1002/mrm.26705.

Figures

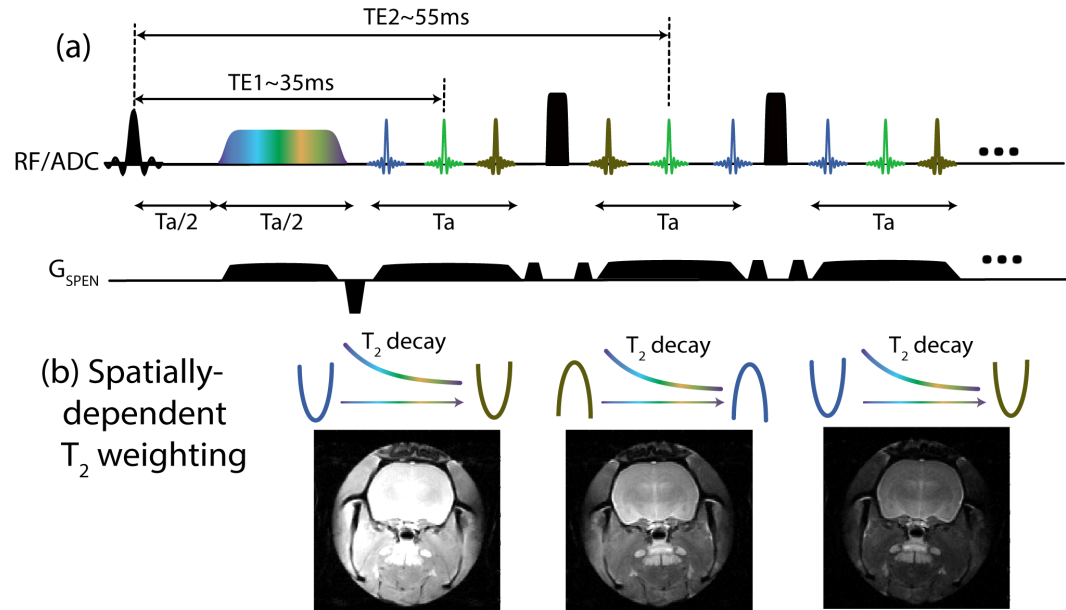


Figure 1. (a) Simplified multi-echo train SPEN pulse sequence omitting the readout and slice selection gradients. The RF/ADC line displays the pulses and signal detection; G_{SPEN} displays the gradients along the SPEN (phase-encoding) axis. The pulse sequence includes the excitation pulse, a delay $T_a/2$ to achieve full refocusing, encoding via a WURST-shaped adiabatic 180° sweep, and a hard or adiabatic 180° pulse to enable multi-echo train acquisition. As the images are sequentially refocused, the echo times differ for different positions (illustrated in turn by the blue, green and brown colors). The sign of the quadratic phase will also be reversed by the hard 180° pulse, leading to the alternating sweep directions as shown in (b). Also shown in (b) are images collected in the different echoes for an *ex vivo* rat head; notice the alternations along the horizontal (y) axes.

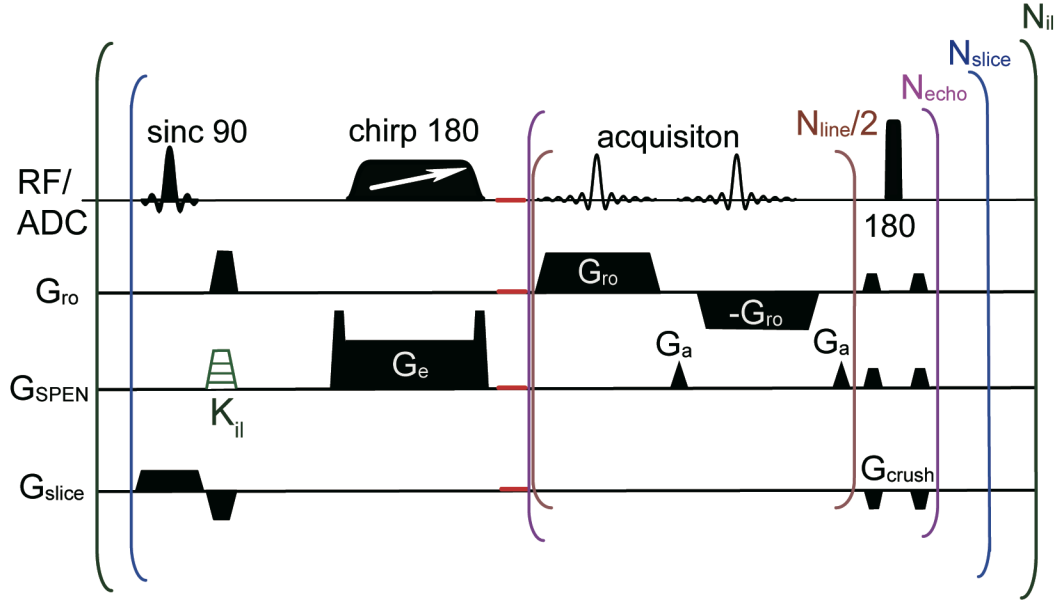


Figure 2. Multislice 2D hybrid MSE-SPEN pulse sequence developed in this study for fast T_2 mapping, composed of four concentric loops. From inner to outer these are an oscillating readout loop, a multi-echo train loop, a multi-slice loop and a multi-shot data interleaving loop; N_{line} , N_{echo} , N_{slice} and N_{il} are the number of SPEN-encoded lines per-shot, the number of echo train, the number of slices and the number of interleaved shots respectively. The RF/ADC line displays the pulses and signal detection; G_{ro} , G_{SPEN} and G_{slice} display the gradients along readout, SPEN (phase-encoding) and slice-selection directions; K_{il} denotes an optional gradient blip used if performing multi-shot interleaving.

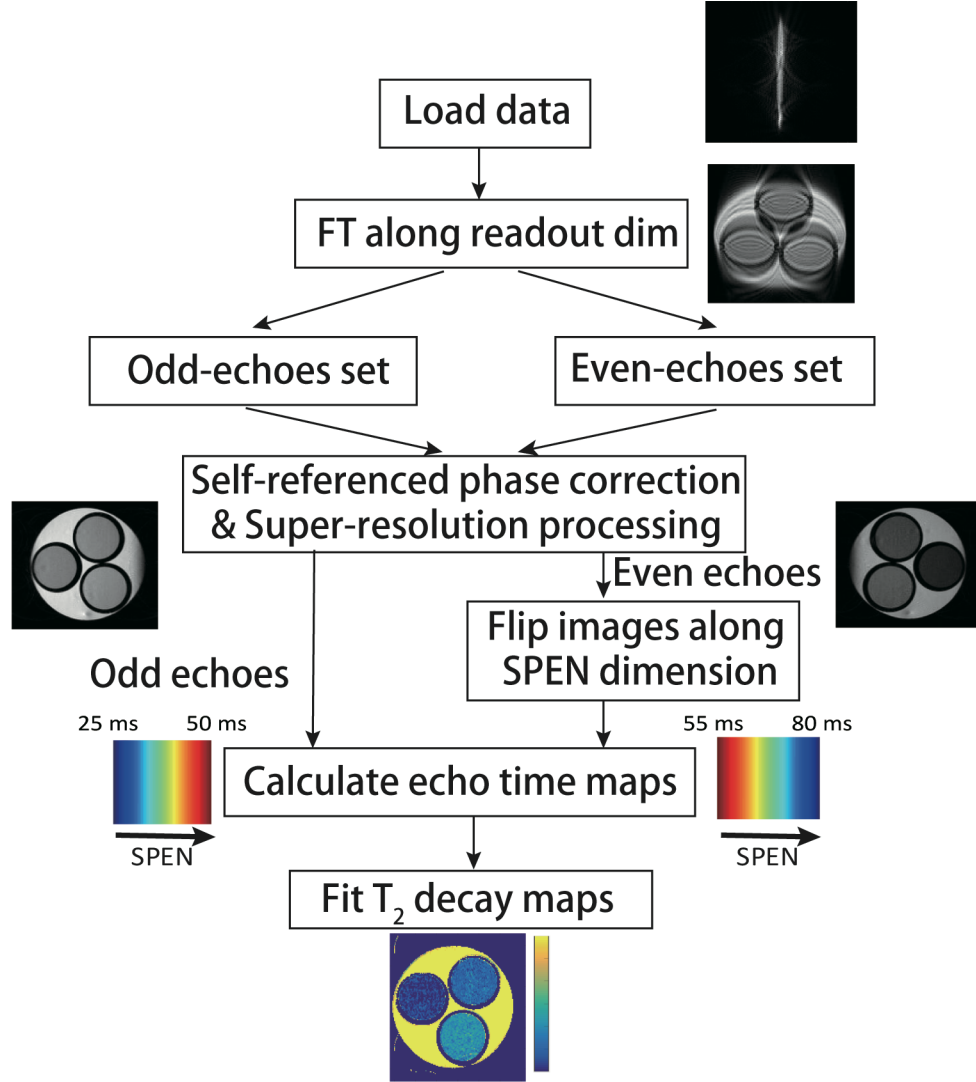


Figure 3. Multislice 2D hybrid MSE-SPEN data processing flow chart developed in this study for fast T_2 mapping, involving a combination of FT and super-resolution procedures as described in Refs. (32,38); for the human brain, where suitable coil geometries and multiple receivers were available, super-resolution in combination with SENSE (36) was implemented to improve the final spatial resolution (the effects of the super-resolution procedure can be appreciated by comparing the images in the 2nd and 4th row of the series). Spatially-dependent echo times were calculated as described in the main text, and mono-exponential fittings were used to calculate the T_2 values in a voxel-by-voxel fashion. Images on the right arise from an actual single-shot T_2 mapping phantom acquisition.

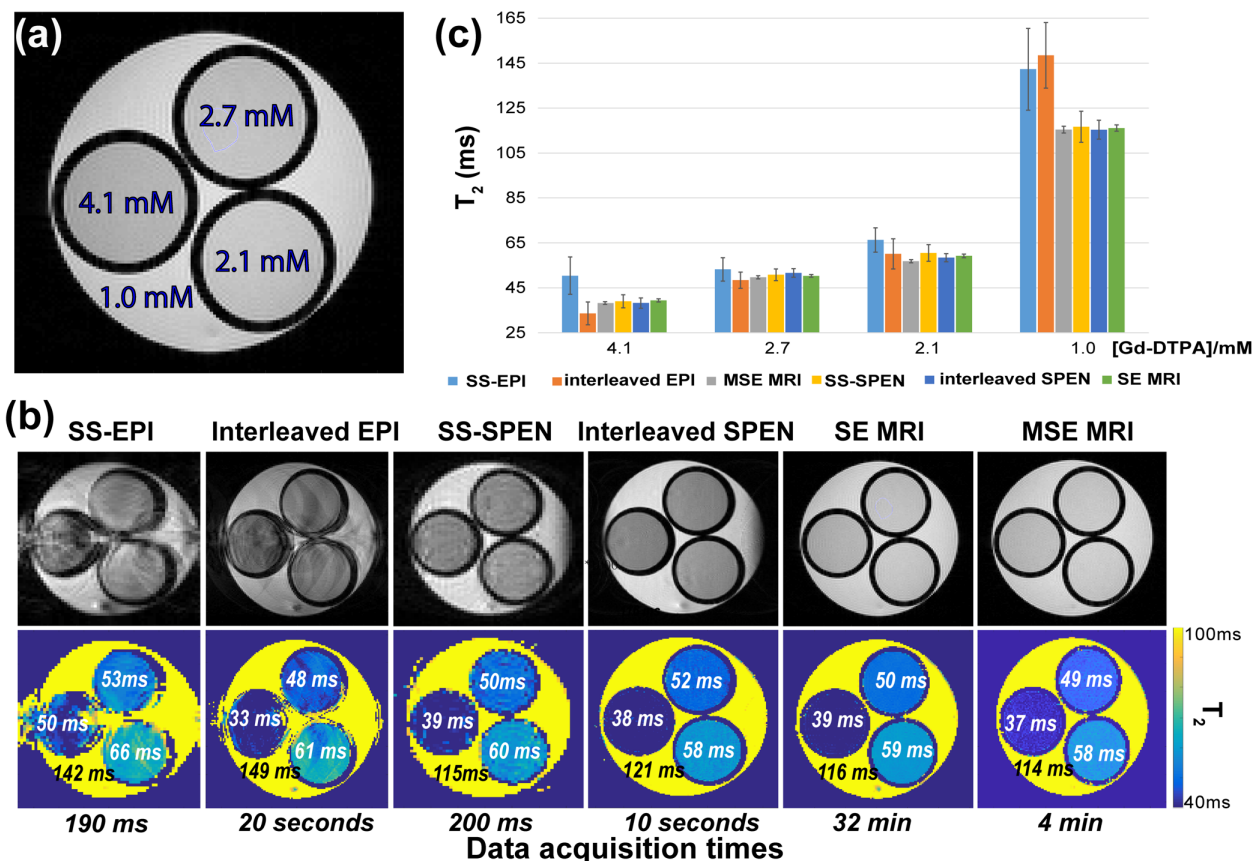


Figure 4. T₂ mapping information arising from the indicated pulse sequences, executed on the phantom shown on panel (a) incorporating tubes with the indicated Gd-DTPA concentration. Panel (b) shows the T₂-weighted images (top) and T₂ maps (bottom) arising from the indicated sequences. Also indicated on the lower line are the total acquisition times required to obtain each T₂ map. In all experiments a single slice 1mm thick was excited. Additional parameters: SS-EPI: resolution=500x500 μm^2 , TE=34ms, MSE train with 7 echoes spaced 25ms apart. Interleaved EPI: 4 shots, in-plane resolution = 250x250 μm^2 , TR/TE=2000/31ms, MSE train with five echoes spaced 24ms apart, one extra reference scan for correcting even/odd effects (leading to the longer EPI vs SPEN scan duration). SS-SPEN: resolution=500x500 μm^2 , TE=36ms, MSE train with 7 echoes spaced 25ms apart, chirp time bandwidth product=120, effective bandwidth~12kHz. Interleaved SPEN: 5 shots, in-plane resolution = 200x200 μm^2 , TR/TE=2000/39ms, MSE train with 7 echoes spaced 28 ms apart, chirp time-bandwidth product=120, effective bandwidth~11kHz. SE MRI: TR/TE=2000/13ms, in-plane resolution = 250x250 μm^2 , TE=8ms. MSE MRI: TR/TE=2000/8.6ms, in-plane resolution = 250x250 μm^2 , 11 echoes with echo space 10ms. Panel (c) are summaries of the average T₂ values arising from the

tubes possessing the indicated Gd-DTPA concentrations, with error bars reflecting the heterogeneities within the tubes. Notice the faithfulness of the single-shot and interleaved SPEN images, and the good agreement between the T_2 values obtained by these techniques and those arising from SE MRI acting as “gold standard”.

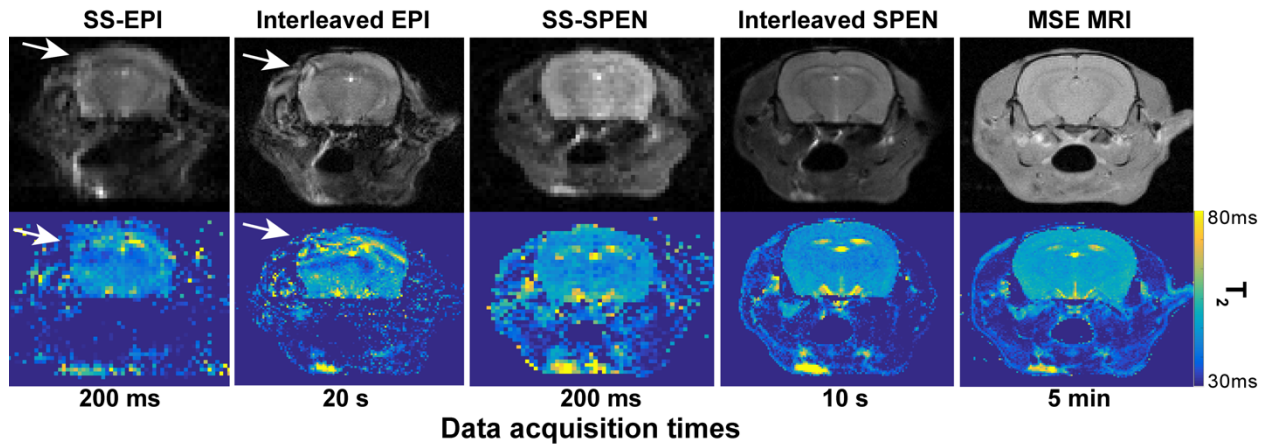


Figure 5. Idem as in Figure 4, but upon comparing T_2 maps for experiments performed on an *in vivo* mouse head: the upper row shows the anatomical images arising from the first-echo data, and the lower row shows hot/cold T_2 maps derived from the scans (the single-spin-echo experiment was skipped owing to its long acquisition time). Slice thickness for all the images was 1 mm. Additional parameters: SS-EPI: resolution= $312 \times 312 \mu\text{m}^2$, TE=34ms, 5 echoes in the train with 25ms spacing. Interleaved EPI: 4 shots plus one extra reference scan (leading to the longer acquisition times) for correcting even/odd effects, in-plane resolution = $156 \times 156 \mu\text{m}^2$, TR/TE=2000/31ms, 5 echoes spaced 24ms. SS-SPEN: resolution= $312 \times 312 \mu\text{m}^2$, TE=36ms, 5 echo train with echo spacing of 25ms, chirp time bandwidth product=120, effective bandwidth~12kHz. Interleaved SPEN: 5 shots, in-plane resolution = $156 \times 120 \mu\text{m}^2$, TR/TE=2000/39ms, 5 echo train with 28 ms spacing, chirp time bandwidth product=120, effective bandwidth~11kHz. MSE MRI: TR/TE=2000/8.6ms, in-plane resolution = $120 \times 120 \mu\text{m}^2$, 11 echoes with echo spacing = 8.6ms. White arrows point towards distortions in the EPI images.

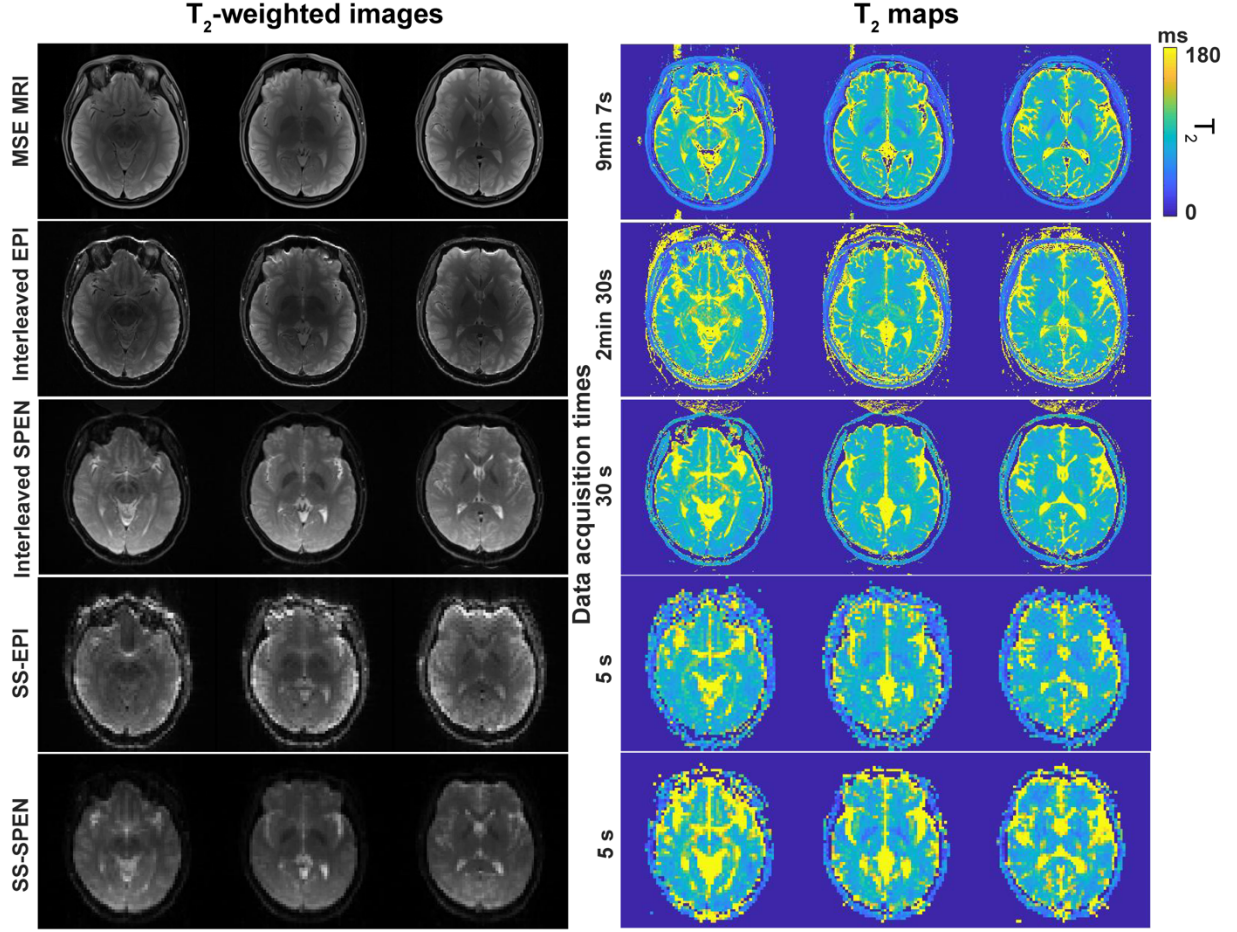


Figure 6. Comparisons of T₂-weighted images (left) and T₂ maps collected on a human brain by a scanner-provided Multi-Spin-Echo sequence (top), and by single-shot/interleaved SPEN and EPI sequences. All sequences collected 5 slices with a slice thickness = 2mm (only three are shown). Additional acquisition parameters: SS-EPI: resolution=3.44x3.44mm², TR/TE=5000/35ms, 5-echo train with 35ms spacing. Interleaved EPI: 5 shots, in-plane resolution = 1.16x1.16mm², TR/TE=5000/39ms, 5 TEs spaced by 39ms were used to obtain T₂ map: no multi-echo train available in the scanner, and hence the longer duration vis-à-vis interleaved SPEN. SS-SPEN: effective in-plane resolution=2.29x2.29mm² reached after multiple-coil (SUSPENSE) interpolation achieved as in Refs. 36 and 37, TR/TE=5000/38.6ms, chirp time-bandwidth product=64, 5 echoes spaced 38.6ms apart. Interleaved SPEN: 5 shots, nominal in-plane resolution (after SUSPENSE) = 0.92x 0.92mm², TR/TE=5000/35.6ms, chirp time-bandwidth product =120, multi-echo train with 5 echoes spaced 35.6 ms. MSE MRI:

TR/TE=5000/32ms, in-plane resolution = $1.15 \times 1.15 \text{mm}^2$, 5 echoes spaced by 32 ms. Indicated next to the T_2 maps are the acquisition times taken by each of the experiments.

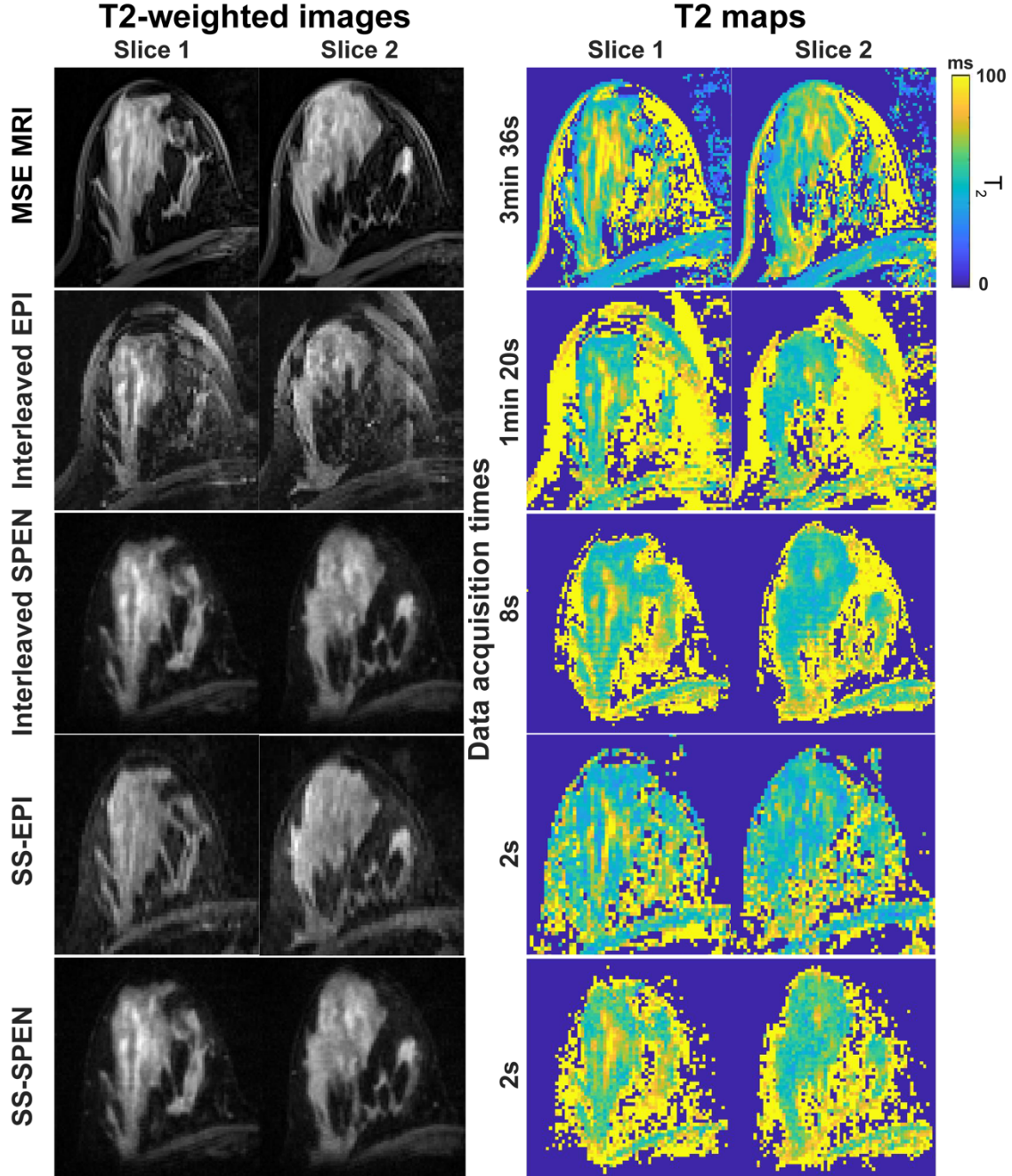


Figure 7. Comparisons between T_2 -weighted images (left) and T_2 maps (right) collected on a human breast by the same sequences as in Figure 6. All sequences collected 2 slices with a 3mm

thickness. Additional acquisition parameters: SS-EPI: resolution= $1.86 \times 1.86 \text{ mm}^2$, TR/TE=2000/27ms, 5-echo train with 27ms spacings. Interleaved EPI: 3 shots, in-plane resolution = $1.33 \times 1.20 \text{ mm}^2$, TR/TE=2000/40ms, 5 TEs spaced 20ms apart. SS-SPEN: resolution= $1.59 \times 1.87 \text{ mm}^2$, TR/TE=2000/63ms, chirp time bandwidth product=64, 5 echoes spaced 44.6ms apart. Interleaved SPEN: 3 shots, in-plane resolution = $1.33 \times 1.20 \text{ mm}^2$, TR/TE=2000/35ms, chirp time bandwidth product = 45, MSE train with 5 echoes spaced 24ms apart. MSE MRI: TR/TE=2000/25ms, in-plane resolution = $1.25 \times 1.25 \text{ mm}^2$, 5 echoes spaced by 25 ms. Indicated as well are the acquisition times taken by each of the experiments.

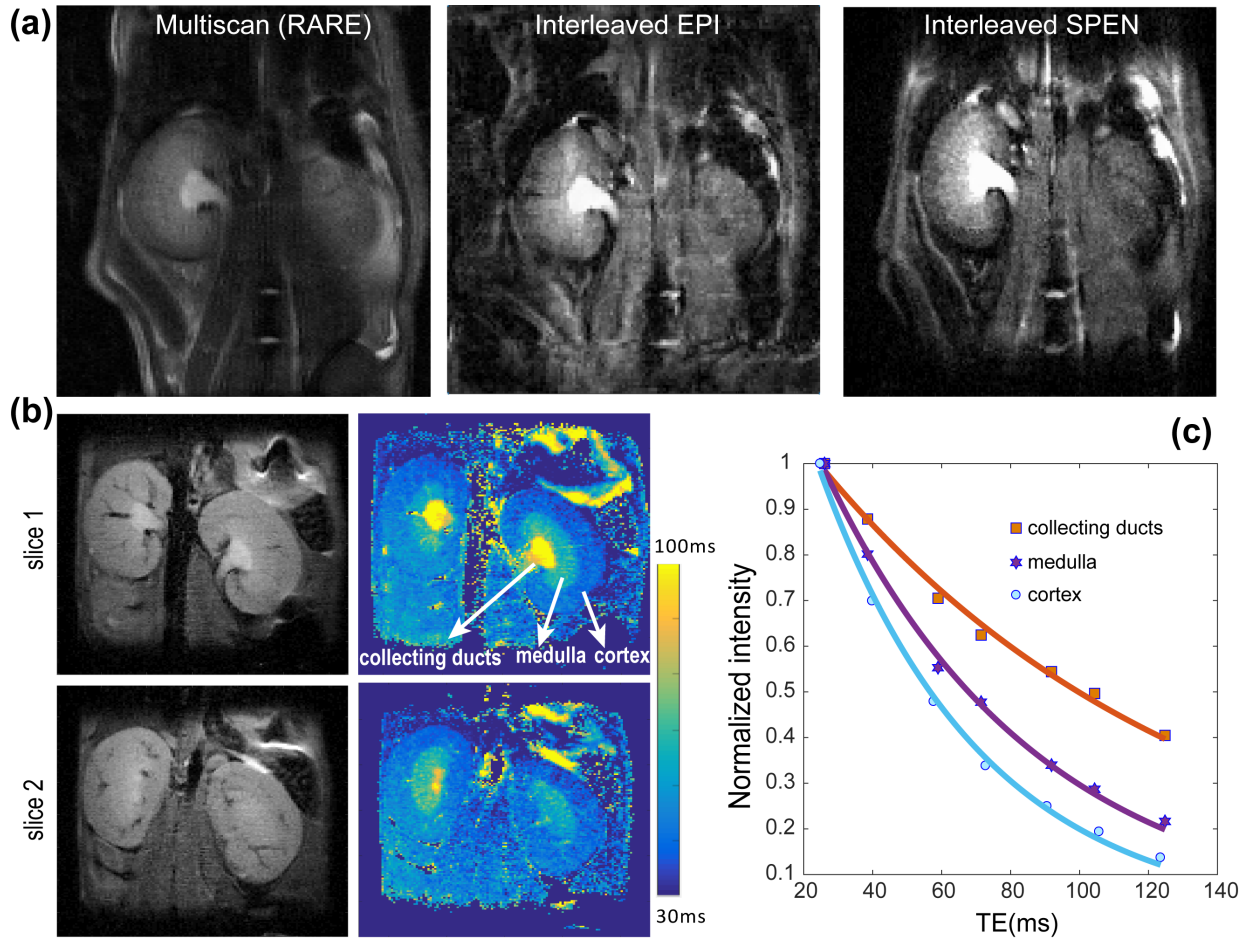


Figure 8. (a) Comparison between different scanning modes applied *in vivo* to T_2 map a mouse abdominal region. Multiscan (RARE) parameters: TR/TE = 2000/48 ms, slice thickness=1mm, in plane resolution: $187 \times 187 \mu\text{m}^2$, echo train length = 8, scan time ≈ 50 sec (with respiratory trigger). Interleaved EPI parameters: TR/TE = 2000/30 ms, slice thickness=1mm, in plane

resolution: $187 \times 187 \mu\text{m}^2$, 5 shots, scan time ≈ 20 sec with respiratory trigger and navigator scan to correct even/odd problems. The stripping in the EPI image arises as a result of imperfect interleaving. Interleaved SPEN parameters: TR/TE = 2000/35 ms, slice thickness=1mm, in plane resolution: $187 \times 187 \mu\text{m}^2$, 5 shots, scan time around 10 seconds with respiratory trigger, no need for reference scan. (b) Multi-slice *in vivo* mouse kidney T_2 mapping by interleaved SPEN; the left column shows the anatomical images and the right one the corresponding T_2 maps collected in ca. 10 sec. Slice thickness =1 mm; 5 interleaved shots collected with respiration trigger, in-plane resolution= $187 \times 187 \mu\text{m}^2$, matrix size=160x160, TR/TE=2000/39ms, 7-echo train with 28ms spacings, chirp time-bandwidth product=120, 4 slices. (c) T_2 decays extracted from three points from different kidney layers (cortex, medulla, collecting ducts) showing clear decay differences.

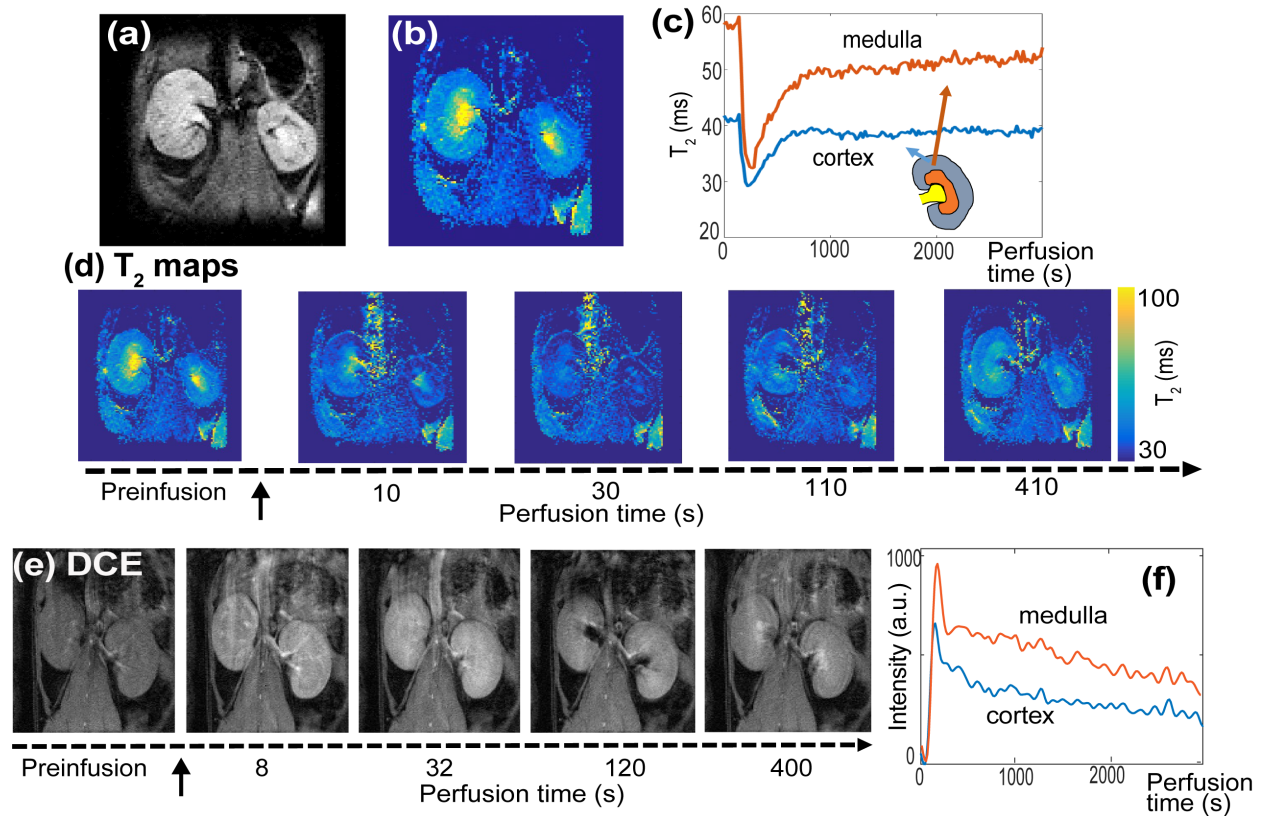


Figure 9. Real time T_2 renal mapping of a live mouse upon injection of a Gd-DTPA bolus (200 μl of 500 mM). (a, b) First echo train image (TE=30 ms) and corresponding T_2 map collected before perfusion of the contrast agent. (c) Dynamic T_2 value curves extracted from a kidney's cortex and medulla regions. (d) Selected T_2 maps extracted at the indicated times after the

injection of Gd-DTPA. These MSE-SPEN data were collected using the following parameters: 5 interleaved shots with respiration trigger, in-plane resolution = $234 \times 250 \mu\text{m}^2$, image size = 128×120 , chirp time-bandwidth product = 120, 1mm slice thickness, TR/TE = 2000/30ms, 5 echoes in the train with an echo spacing of 28 ms. (e, f) Time series images and dynamic intensity changes obtained from T₁-weighted gradient echo experiments collected using the following parameters: 1mm slice thickness, TR/TE = 30/3.3ms, in-plane resolution = $234 \times 250 \mu\text{m}^2$, image size = 128×128 , 2 averages. Black arrows indicate the time of Gd injection.

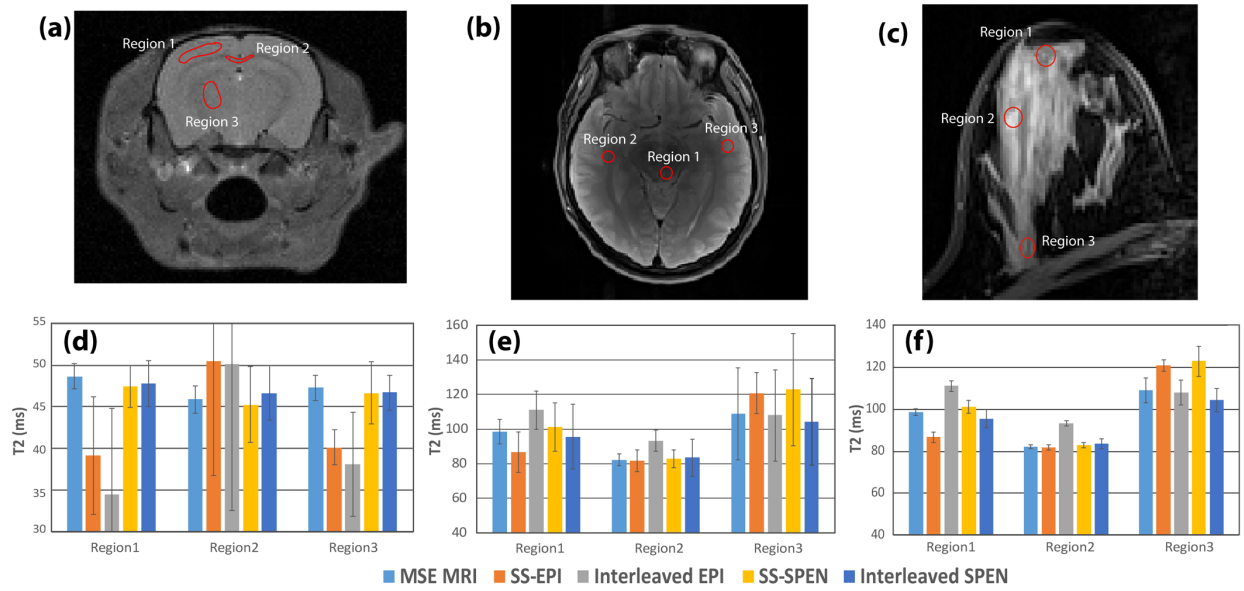
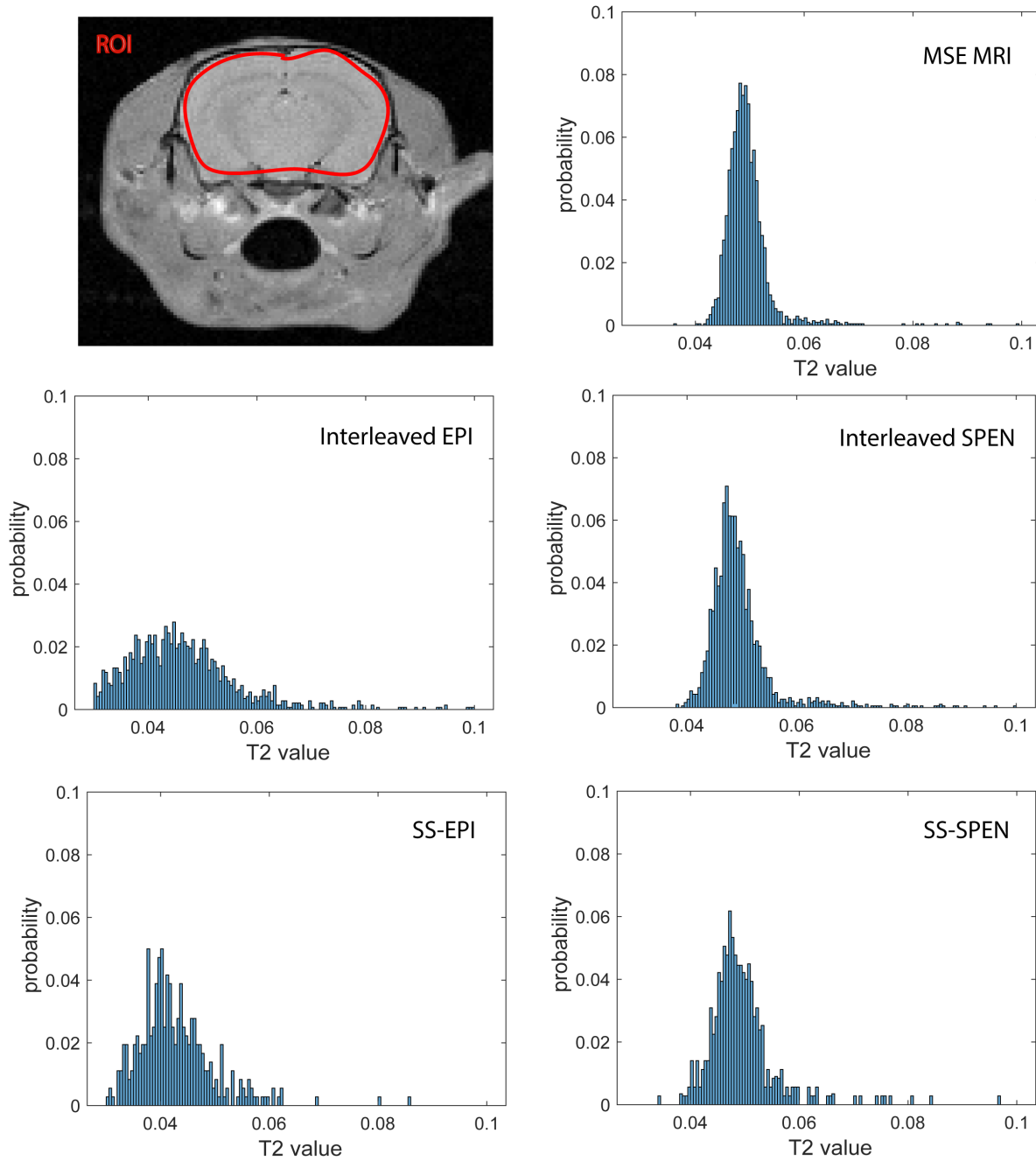
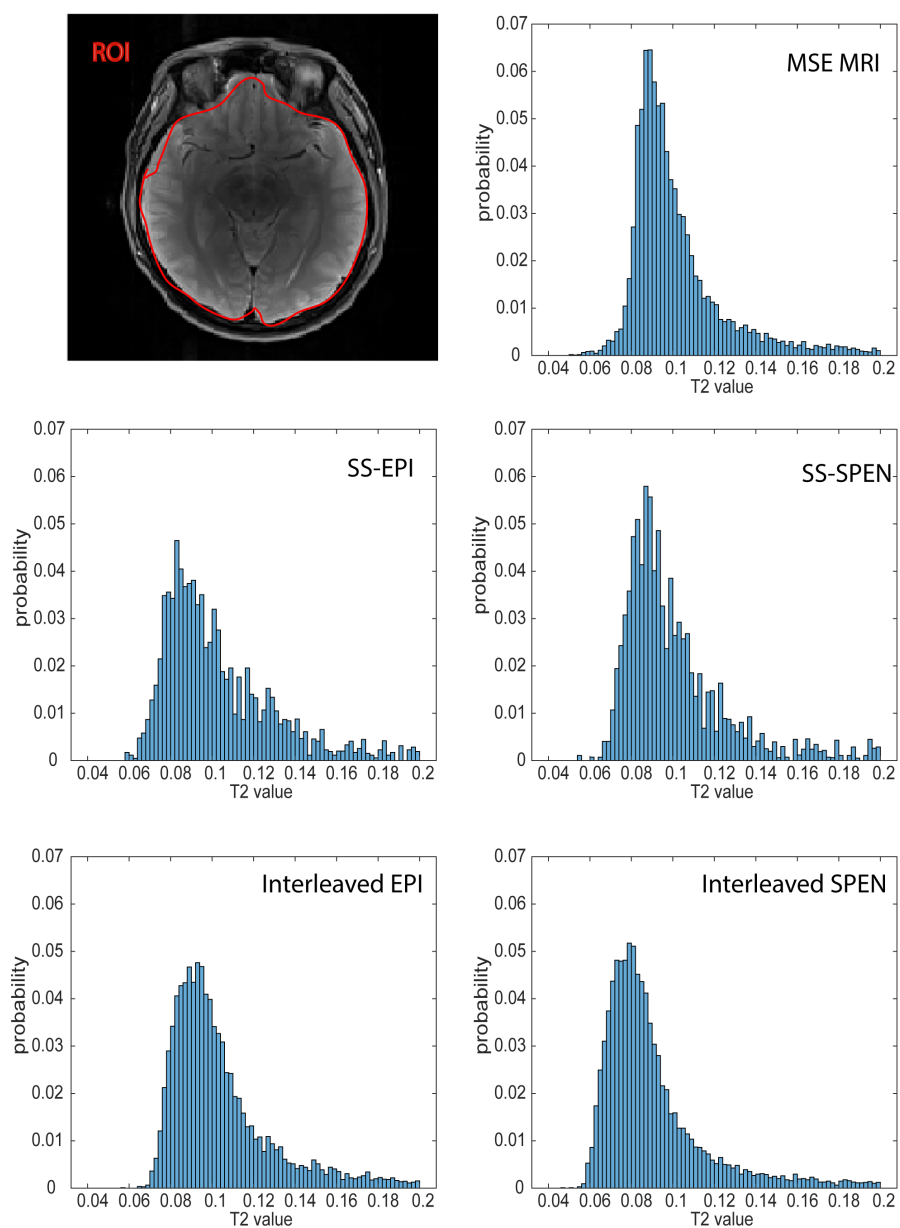


Figure 10. Comparing T₂ values in different ROIs arising from *in vivo* experiments performed on a mouse brain (a, d), on a human brain, (b, e) and on a human breast (c, f). The upper row shows the positions of the different ROIs selected for the comparisons, and the lower row shows the T₂ values obtained from the data presented in Figs. 5-7, comparing the results provided by the different sequences tested. Error bars in each plot reflect the distributions of T₂s about their average, detected for each ROI. See Supporting Information Figures S1 and S2 for a more detailed comparison of these summaries.



Supporting Figure S1. Comparison of the T₂ value distributions arising from the different pulse sequences assayed in this work, as applied to the indicated brain ROI of *in vivo* mice experiments (Fig. 5).



Supporting Figure S2. Comparison of the T_2 value distributions arising from the different pulse sequences assayed in this work, as applied to the indicated brain ROI from *in vivo* human scans (Fig. 6).